# Photoproduction of $\eta$ mesons off protons for $E_\gamma \leqslant 1.15$ GeV

T. Nakabayashi,[1] H. Fukasawa,[1] R. Hashimoto,[1] T. Ishikawa,[1] T. Iwata,[2] H. Kanda,[3] J. Kasagi,[1] T. Kinoshita,[1] K. Maeda,[3]
F. Miyahara,[1] K. Nawa,[1] T. Nomura,[2] H. Shimizu,[1] T. Shishido,[2] K. Suzuki,[1] Y. Tajima,[2] T. Takahashi,[4] H. Ueno,[2]
H. Yamazaki,[1] and H. Y. Yoshida[2]

[1]*Laboratory of Nuclear Science, Tohoku University, Sendai 982-0826, Japan*
[2]*Department of Physics, Yamagata University, Yamagata 990-8560, Japan*
[3]*Department of Physics, Tohoku University, Sendai 980-8578, Japan*
[4]*High Energy Research Organization (KEK), Tsukuba 305-0801, Japan*

$\eta$ mesons emitted from the photoproduction off protons were measured for $0.70 \leqslant E_\gamma \leqslant 1.15$ GeV. The $\gamma p \to \eta p$ reaction process was separated from the $\pi \eta p$ final state by the momentum difference of $\eta$ mesons for $E_\gamma \geqslant 930$ MeV. The angular distributions obtained and the excitation function of the $\gamma p \to \eta p$ reaction are essentially in good agreement with previously reported ones and are well explained by $\eta$-MAID calculations. For the $\gamma p \to \pi \eta N$ reaction, the cross section increases monotonically with increasing photon energy, and it almost reaches the value of the $\gamma p \to \eta p$ reaction at $E_\gamma \sim 1.15$ GeV. The momentum distributions are compared with kinematic calculations. It is suggested that the sequential decay process through the $P_{33}(1232)$ resonance $[\gamma p \to \eta P_{33}(1232) \to \pi \eta N]$ contributes to the $\gamma p \to \pi \eta N$ reaction, in addition to the sequential process $\gamma p \to \pi S_{11}(1535) \to \pi \eta N$ and/or $\pi$ and $\eta$ emissions without intermediate nucleon resonances.

## I. INTRODUCTION

Recently, the $\gamma p \to \eta p$ reaction has been extensively measured over the entire energy region of the so-called second and third nucleon resonances [1–6]. These data, which include angular distributions, polarized beam asymmetry, polarized target asymmetry, and the excitation function of the total cross section, have prompted detailed theoretical analyses [6–8] and have revealed the complex structure of $N^*(I = 1/2)$ for photoexcitations followed by the $\eta$ emission.

It was found that in addition to the strongly contributing $S_{11}(1535)$ resonance, other weakly excited resonances contributed to the cross section through the interference terms; the effects were small but evident. Although the data from Mainz [1], GRAAL [4], JLab [5], and Bonn [6] are in good agreement with each other, small discrepancies exist in the total cross section as well as in the angular distribution. For example, the excitation function reported in [4] shows a slight increase at $E_\gamma \geqslant 1000$ MeV, and the angular distributions show forward peaking. The possible existence of a third $S_{11}$ resonance was proposed in [7]; however, the analysis of the most recent data in [6] did not require a third $S_{11}$ resonance in this energy region.

We report on the measurement of $\eta$-meson emissions in the photon-induced reaction on protons for photon energies up to 1.15 GeV. One important motivation of the present experiment was to deduce the cross section for the $\gamma p \to \pi \eta N$ reaction, which allows us to better analyze data for the C,Cu$(\gamma, \eta)$ reactions [9]. Thus, we present and discuss the cross section of the $\gamma p \to \pi \eta N$ process in detail, for the first time, in addition to discussing the discrepancies between different experiments in the cross section of the $\gamma p \to \eta p$ reaction.

## II. EXPERIMENTAL PROCEDURE

The experiments were performed at the Laboratory of Nuclear Science (LNS) at Tohoku University. A $\gamma$ beamline with a new tagged photon system was constructed for the GeV-$\gamma$ experimental hall where the present experiment was carried out. The new improved system realized better time resolution and higher counting rates than the previous one [10]. Figure 1 shows the experimental setup. Tagged photons are produced by a thin carbon fiber radiator placed in the 1.2 GeV stretcher-booster ring (STB), pass through 10 m of air, enter a vacuum chamber in front of the charge sweeping magnet, and hit the solid hydrogen target downstream. The photon energy was covered from 580 to 880 MeV with electron beam energy $E_e = 920$ MeV and from 750 to 1160 MeV with $E_e = 1.2$ GeV. The total tagged photon intensity was about $2 \times 10^7$ photons/s, and photon beam profiles were checked regularly during the experiment with a beam profile monitor. The size of the beam at the target position was about 5 mm (rms). The transmission efficiency of tagged photons, which is the ratio of the number of photons impinging on the target to the number of recoiling electrons detected by a tagging detector, was measured frequently by using a lead glass detector for photon detection placed on the photon beamline. The transmission efficiency obtained was close to 55% and very stable (within $\pm$ 1.5%) during the experiment.

The solid hydrogen target was encased in a rectangular prism-shaped container (40 mm wide, 50 mm high, and 80 mm long) placed in a vertically cylindrical vacuum chamber made of stainless steel with a diameter of 170 mm and a wall thickness of 2 mm. The container itself was made of 3-mm-thick aluminum and had 50-$\mu$m-thick Mylar foil windows 35 mm in diameter on both entrance and exit sides for the photon beam to pass through. It was fixed directly onto the
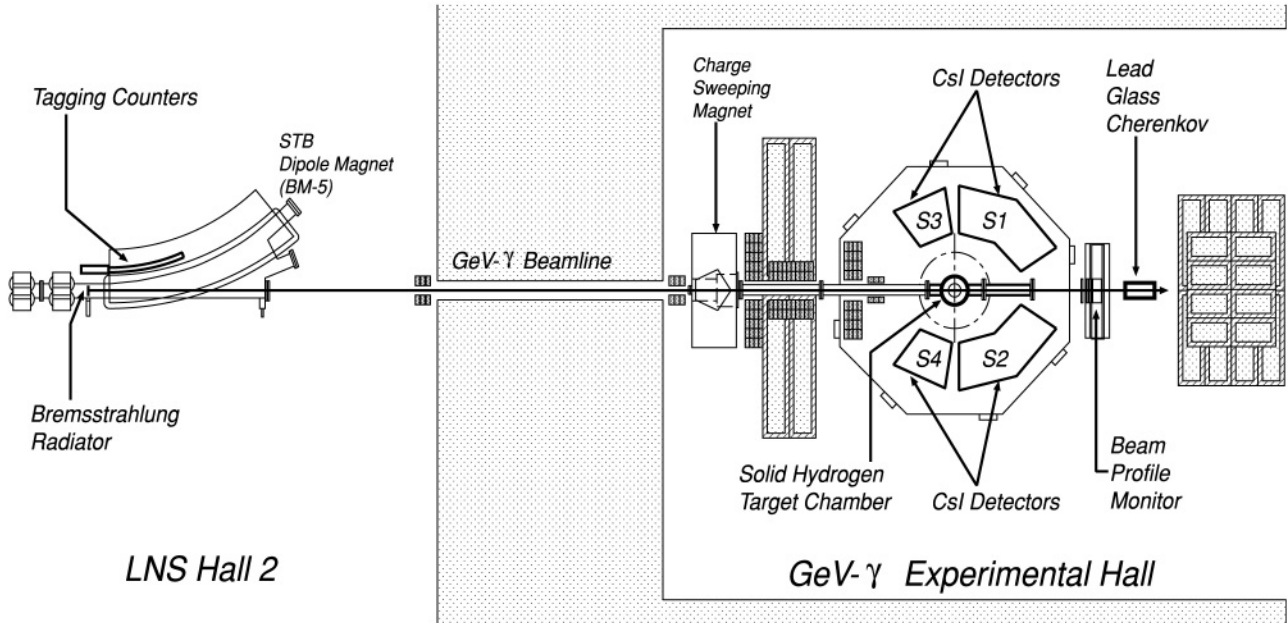
FIG. 1. Experimental setup at GeV-$\gamma$ experimental hall in LNS.

second stage (4 K) of the GM refrigerator (Sumitomo SRDK-408D) and surrounded by a radiation shield (0.5-mm-thick Al foil) connected to the first stage (30 K). The condition of the solid hydrogen was monitored online by measuring the vacuum pressure of the chamber and the temperature of the container during the run: they were kept to less than $10^{-7}$ torr and below 8.5 K, respectively. The background events from the Mylar windows of the container were measured separately without hydrogen in the container.

Two photons from an $\eta$ meson were detected by an electromagnetic calorimeter consisting of 206 pure CsI crystals with plastic scintillation counters. Each crystal was shaped like a truncated hexagonal pyramid with a thickness of 300 mm for 148 pieces (type A) and 250 mm for 58 pieces (type B): the performance of the type-B detector is described in detail in [11]. The detectors were assembled in four blocks so that two sets of 74 crystals of type A covered the forward angles of $15° \leqslant \theta \leqslant 72°$ with respect to the beam direction for both sides of the beam and angles of $-17° \leqslant \phi \leqslant 17°$ with respect to the horizontal plane (shown as S1 and S2 in Fig. 1). The two sets of 29 type-B crystals covered backward angles of $95° \leqslant \theta \leqslant 125°$ and $-12° \leqslant \phi \leqslant 12°$ (shown as S3 and S4 in Fig. 1). Plastic scintillators, 5 mm thick, placed in front of the CsI crystals served for charged-particle identification.

The data were collected using a data acquisition system similar to the one reported in [12]. The main trigger for the data acquisition required at least one signal from the tagging counters and two signals from the CsI detectors. The threshold level of the discriminator for each CsI detector was set at 10 MeV. The maximum counting rate of individual counters was 1 kHz for the CsI and 500 kHz for the tagging counter. A time resolution for $e$-$\gamma$ coincidence events of 500 ps was achieved, and the chance coincidence ratio was about 20%.

## III. DATA ANALYSIS

In the off-line analysis, events to be analyzed were required to have at least two photons detected simultaneously, which were discriminated from incident charged particles and neutrons by referring to the pulse height signal of the plastic scintillator as well as the time-of-flight information. Events with two photons were classified as 2-$\gamma$ events and those with three or more photons as multi-$\gamma$ events. The selected events were then classified as events with and without accompanying charged particles.

Energy and direction of a detected $\gamma$ ray were obtained as follows. A CsI scintillator in which the maximum energy was deposited was selected as the center, and the amount of energy deposited by one photon was obtained by summing up the energies of the surrounding six CsI scintillators as described in [12]. An energy-weighted central position was calculated and taken to be the incident position of the photon at the detector surface. At 1-GeV photon energy, $\Delta E_\gamma = 30$ MeV and $\Delta\theta = 2.1°$ were obtained.

To obtain the $\eta$-meson yield, the momentum of a particle decaying to two $\gamma$ rays was derived from detected two-photon events, and the event was sorted out into a bin with an angle step $\Delta\cos\theta^{\text{c.m.}} = 0.2$ and momentum step $\Delta p^{\text{c.m.}} = 20$ MeV/$c$ in the center-of-mass system. Then the invariant mass spectrum was constructed for all bins. Figure 2 shows examples deduced for $0.8 \leqslant \cos\theta^{\text{c.m.}} \leqslant 1.0$ at $E_\gamma = 814$ MeV. Figure 2(a) is for $100 \leqslant p^{\text{c.m.}} \leqslant 140$ MeV/$c$, and Fig. 2(b) is for $220 \leqslant p^{\text{c.m.}} \leqslant 260$ MeV/$c$. Since the c.m. momentum of the $\eta$ meson emitted in the $\gamma p \to \eta p$ reaction at $E_\gamma = 814$ MeV is 240 MeV/$c$, a peak corresponding to the invariant mass of 550 MeV is seen clearly in Fig. 2(b), whereas only continuum events appear in Fig. 2(a). The continuum background events on which the $\eta$-meson events are superimposed originate mainly from multi-$\pi^0$ emission. The $\eta$-meson yield in each

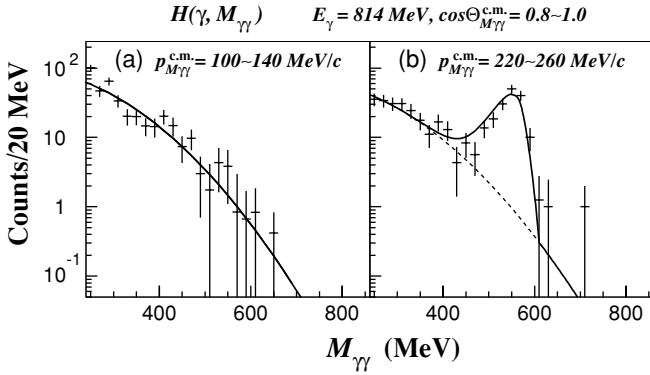FIG. 2. Invariant mass spectrum of two photons for $E_\gamma = 814$ MeV, $0.8 \leqslant \cos\theta^{c.m.} \leqslant 1.0$, and $p^{c.m.}$ as shown in (a) and (b). In (a) the result of fitting for background events is shown by the solid line. Solid line in (b) shows the result of the fitting for the $\eta$-meson peak with the background; dashed line indicates the background part.

spectrum was deduced by subtracting the background in the $\eta$ mass region estimated by the function $AF(M_{\gamma\gamma}) + B\exp(aM_{\gamma\gamma}^2 + bM_{\gamma\gamma})$, fitted to the yield by adjusting $A$, $B$, $a$, and $b$ as shown in Fig. 2(b). Here, the first term accounts for the broad peak with an asymmetric tail presented by a Landau distribution function $F(x) = \exp[-(R(x_0 - x) + e^{-R(x_0-x)})/2]$ with $R = 0.04$ (width parameter) and $x_0 = 550$ (peak position), and the second term represents the background. Zero peak yields were obtained in the kinematically forbidden region as shown in Fig. 2(a), where the background function alone provides a good fit to the data.

The cross section of the $\gamma p \to \eta p$ reaction was deduced only from 2-$\gamma$ events in the entire $E_\gamma$ region. However, the cross section of the $\gamma p \to \pi\eta N$ reaction, which is open for $E_\gamma \geqslant 930$ MeV, was deduced from both 2- and multi-$\gamma$ events. In Fig. 3, the yields of $\eta$ mesons vs the c.m. momentum at $E_\gamma = 1050$ and $1080$ MeV are shown. The peak at $430$ MeV/$c$ corresponds to $\eta$ mesons emitted in the $\gamma p \to \eta p$ reaction,
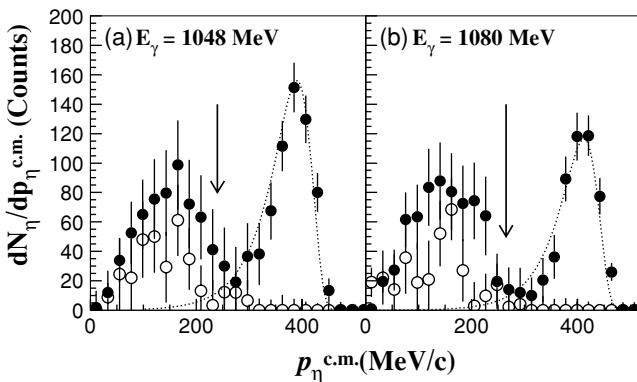


FIG. 3. Yields of $\eta$ mesons vs momentum in the c.m. system at $E_\gamma = 1048$ and $1080$ MeV. Closed circles are deduced from 2-$\gamma$ events and open circles from multi-$\gamma$ events. Arrow indicates the maximum momentum available for the $\gamma p \to \pi\eta N$ reaction. Dotted line shows the line shape of the $\eta$ mesons emitted in the $\gamma p \to \eta p$ reaction simulated for the present experimental system.

and the arrow indicates the maximum momentum allowed for events emitted in the $\gamma p \to \pi\eta N$ reaction. As expected, the 2-$\gamma$ events (closed circles) appear in the entire momentum range, whereas the multi-$\gamma$ events (open circles) appear only in the low-momentum region below the arrow. Thus, the two reaction processes are well distinguished in the present experiment. The dotted line is the response of the present detector system calculated with a Monte Carlo simulation code for the $\gamma p \to \eta p$ reaction at $E_\gamma = 1050$ and $1080$ MeV: the observed line shape of the peak is well reproduced.

The $\eta$-meson yield in each bin was converted into a relative cross section by using the acceptance of the present detector system, which was estimated by a GEANT3 [13] based Monte Carlo simulation. The acceptance calculation included geometry and materials of the hydrogen target setup, the vacuum chamber, and the CsI detector system. Low energy threshold levels of individual detectors were included as well. Absolute cross sections were then deduced by taking into account the thickness of the hydrogen target, tagging counter counts, photon transmission efficiency, and branching ratio of 2-$\gamma$ decay of the $\eta$ meson [14]. The systematic errors of the overall normalization were due to uncertainties in photon flux (2%), the number of the target protons (1%), background determination (4%), and detector acceptance (3%). Consequently, the total systematic error was about 6%.

In addition, the cross section of the $\gamma p \to \pi^0\eta p$ reaction was deduced by analyzing 2- and multi-$\gamma$ events accompanied by a charged particle. Accompanying proton events produced a locus on the $\Delta E$-$E$ two-dimensional plot for the plastic and CsI detector. They were well separated from the ones originated from $\pi^+$ and $e^\pm$, and thus, events for the $\pi^0\eta p$ final state could be well identified. However, sorting coincident proton events into the small bins reduced the number of events to less than 1/10 of the inclusive $\eta$ events. Therefore, only the total yield for the $\eta$ mesons at each incident photon energy was deduced from the invariant mass spectrum constructed from the events with $p_\eta^{c.m.}$ below the maximum momentum of the $\gamma p \to \pi^0\eta p$ reaction. In this case, the acceptance was estimated using the assumption that the $\pi^0$ and $\eta$ mesons and the proton were emitted in accordance with a constant distribution in the phase space of the final state.

## IV. RESULTS AND DISCUSSION

### A. $\gamma p \to \eta p$ reaction

In the same energy region, good quality data that have been reported recently for the $\gamma p \to \eta p$ reaction essentially agree with each other [1,4–6]. Thus, it is established that the main contribution to the total cross section for $E_\gamma \leqslant 900$ MeV originates from the $S_{11}(1535)$ resonance. However, small discrepancies occurring in experimental data just around 1000 MeV have caused a controversy as to whether other resonances contribute to the data. Therefore, we concentrate our discussion on data above $E_\gamma \geqslant 930$ MeV.

In Fig. 4, the angular distributions are shown for several photon energies. The present results are plotted along with data measured in other laboratories at the nearest photon energy.
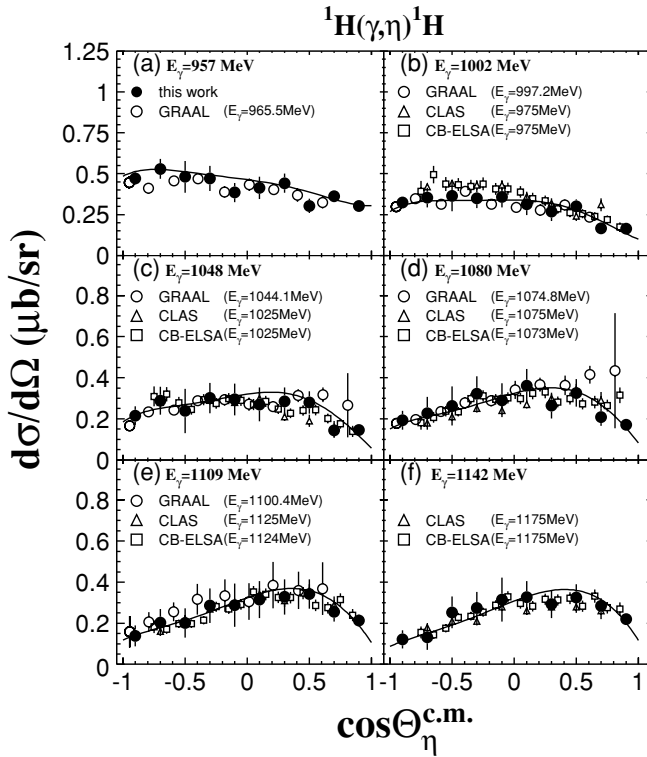
FIG. 4. Angular distributions for $\eta$ emission in $\gamma p \to \eta p$ reaction for photon energies higher than 930 MeV. Present results are plotted with solid circles; those measured in other laboratories are also shown at the nearest photon energy: open circles from GRAAL [4], triangles from JLab [5], and squares from Bonn [6]. Solid line is the result of $\eta$-MAID [8] calculations.

Although all data are in good agreement, small discrepancies remain. In Fig. 4(b), the data from JLab [5] and Bonn [6] are systematically larger than those from GRAAL [4] and the present results. This is probably due to the small difference in incident photon energies, since the angular distribution pattern is changing rather rapidly with increasing photon energy. The agreement between the present results and those from GRAAL is very good except for the data at $E_\gamma = 1048$ and 1080 MeV. The cross sections at the two most forward angles are slightly larger in GRAAL [4]; however, the error bar is excessively large for the most forward angle. At the latter energy, a slight deviation from our results is also seen at the most forward angle in the data from Bonn [6]. Solving this inconsistency at the most forward angles might be important for the interpretation of the $S_{11}$ resonances, since Saghai and Li [7] proposed the existence of a third $S_{11}$ resonance at 1100 MeV, which would result in the angular distribution being forward peaking as observed in the GRAAL data [4,7]. The solid curve in Figures 4(a)–4(f) is the result of an $\eta$-MAID [8] calculation in which two $S_{11}$ resonances, $S_{11}(1535)$ and $S_{11}(1650)$, are included but not a third $S_{11}(1700)$ resonance. Note that the present data are well reproduced by the $\eta$-MAID [8] calculation.

In Fig. 5, the excitation function of the total cross section is plotted, showing the present results and data from the other laboratories. Up to 1020 MeV, all data agree very well; but
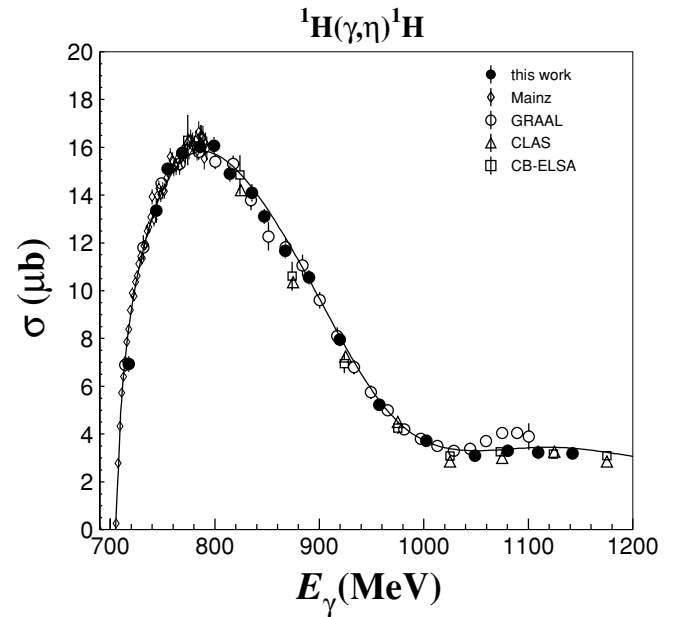


FIG. 5. Excitation function of cross section for $\gamma p \to \eta p$ reaction. Solid circles show the present result, open circles from GRAAL [4], triangles from JLab [5], squares from Bonn [6], and diamonds from Mainz [1]. Solid line is the $\eta$-MAID [8] calculation.

above $E_\gamma \geqslant 1040$ MeV, the present results are very close to those of Bonn [6] and JLab [5] but slightly smaller than those of GRAAL [4]. This discrepancy is linked to the difference in angular distribution data at very forward angles. Including a third $S_{11}$ resonance as suggested by Saghai and Li [7] would result in a slight increase in the cross section with increasing photon energy as seen in the GRAAL data [4]. However, the present data show no increase in the cross section in this energy region and are well reproduced by the $\eta$-MAID [8] calculation, which is plotted in Fig. 5 with a solid line. In this calculation, the main contribution to the cross section is from the $S_{11}(1535)$ resonance, but its amplitude interferes destructively with the $S_{11}(1650)$ resonance. This results in a practically constant cross section for $E_\gamma \geqslant 1000$ MeV.

The $\eta$-MAID [8] calculation also overestimates the cross sections for $820 \leqslant E_\gamma \leqslant 880$ MeV when we compare the present results with the calculation in detail, although the largest discrepancy is less than 1 $\mu$b at around $E_\gamma = 850$ MeV. It seems that the data fall consistently below the $\eta$-MAID calculation in this energy region. To improve the fit, it might be important to determine the resonance parameters of the $S_{11}(1535)$ and $S_{11}(1650)$ resonances to higher accuracy.

### B. $\gamma p \to \pi \eta N$ reaction

Momentum distributions of the $\eta$ mesons deduced in the present work are shown in Fig. 6. As already mentioned, the peaks at higher momenta correspond to the $\eta$ mesons emitted in the $\gamma p \to \eta p$ reaction. In the low momentum region, yields are continuously distributed up to the maximum momentum available in the $\pi \eta N$ final state. Angular distributions for these low momentum $\eta$ mesons are shown in Fig. 7. They
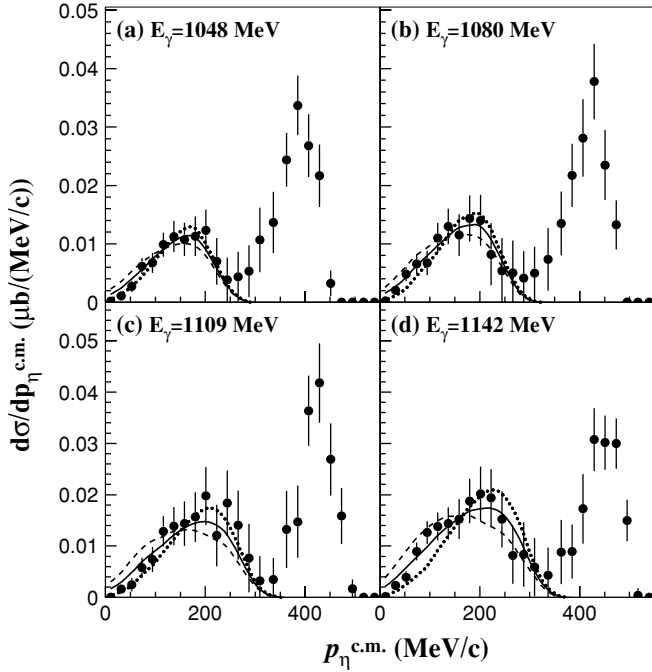
FIG. 6. Momentum distributions of $\eta$ mesons emitted in the $\gamma p \to \pi \eta N$ reaction, for four different $E_\gamma$ . Lines correspond to kinematic calculations: dotted line for process (1) $\gamma p \to \pi \eta N$ and/or (2) $\gamma p \to \pi S_{11}(1535) \to \pi \eta N$; dashed line for process (3) $\gamma p \to \eta P_{33}(1232) \to \pi \eta N$. Solid line corresponds to the calculation in which process (3) contributes 50% of the total yield.



FIG. 7. Angular distributions of $\eta$ mesons emitted in the $\gamma p \to \pi \eta N$ reaction. Solid line shows an isotropic distribution.

are consistent with an isotropic distribution, as shown by a solid line.

The momentum distributions are compared with a simplified kinematic calculation. The following three processes to produce the $\pi \eta N$ final state are considered in the calculation: (1) emission of $\pi$ and $\eta$ mesons without intermediate nucleon resonances, (2) sequential decay through the $S_{11}(1535)$ resonance [$\gamma p \to \pi S_{11}(1535) \to \pi \eta N$], and (3) sequential decay through the $P_{33}(1232)$ resonance [$\gamma p \to \eta P_{33}(1232) \to \eta \pi N$]. In process (1), the initial photon is absorbed by the proton and the $\pi$ and $\eta$ mesons are emitted without intermediate resonances. In this case the differential cross section may be described as $d\sigma \propto$ (PS), where (PS) stands for the phase space of the final state. In processes (2) and (3), the system emits the $\pi$ or $\eta$ meson first, populating the $S_{11}(1535)$ or $P_{33}(1232)$ resonance, and subsequently this resonance decays to the nucleon by emitting the $\eta$ or $\pi$ meson. In this case, the intermediate resonance modifies the simple phase-space distribution, since the cross section can be expressed as $d\sigma \propto |D_{S_{11}(P_{33})}|^2 \times$ (PS). Here, $D_{S_{11}(P_{33})}$ stands for a propagator of the resonance, which is dominated by the denominator, i.e., $D_{S_{11}(P_{33})} \propto [(p_{\pi(\eta)} + p_N)^2 - m_{S_{11}(P_{33})}^2 + i m_{S_{11}(P_{33})} \Gamma_{S_{11}(P_{33})}]^{-1}$, where $m_i$ and $\Gamma_i$ are the mass and width of the resonance, respectively. Thus, for process (1), the differential cross section depends only on the phase space of the final state. For processes (2) and (3), the cross section is proportional to the product of the resonance shape and the phase space.

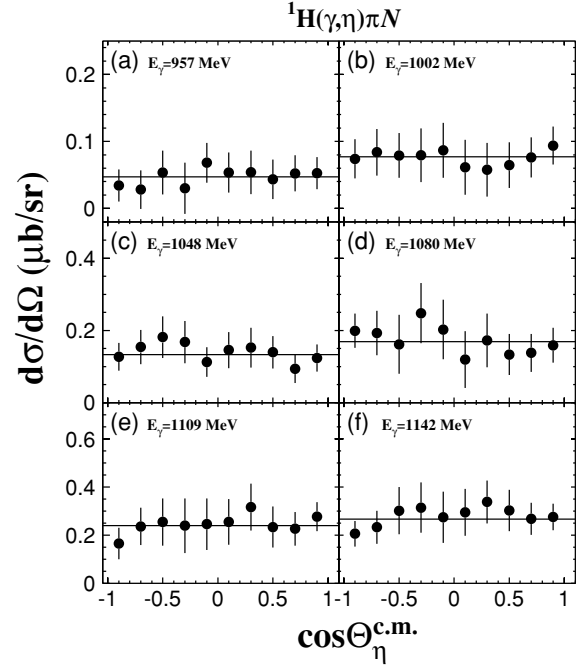Results of the calculation, which are folded with the response function of the detector system, are shown in Fig. 6.

Dotted lines correspond to the process (1) and dashed lines to (3). Both lines are normalized to the integrated cross section at the photon energy. Process (2) is not shown here because it results in a distribution similar to process (1). In view of the large uncertainties in the data, both calculations seem to reproduce the data well. However, fits to the data are worse at higher photon energies. The dotted line underestimates the yield in the low momentum region $p_\eta^{c.m.} \leqslant 150$ MeV/$c$, in particular the data at $E_\gamma = 1142$ MeV. On the other hand, the dashed line underestimates the yield at around $p_\eta^{c.m.} = 200$ MeV/$c$. As a consequence, the $\chi$-squared values, which are 0.44 and 0.32, respectively, for the dotted and the dashed lines at $E_\gamma = 1080$ MeV, become 1.76 and 3.2, respectively, at $E_\gamma = 1142$ MeV. Since deviations in the two distributions lead to compensation at higher energies, a mixture of process (1) and/or (2) together with process (3) might give better fits to the data. For example, the solid line is a calculation for a mixture of 50% process (1) with 50% process (3). This mixture obtains a much better fit to the experimental distribution, resulting in smaller $\chi$-squared values, 0.12 at $E_\gamma = 1080$ MeV and 0.54 at $E_\gamma = 1142$ MeV. Thus, it is suggested that the reaction $\gamma p \to \pi \eta N$ proceeds partly through the sequential process $\gamma p \to \eta P_{33}(1232) \to \pi \eta N$ in this energy region, although the possibility that process (1) and/or (2) is the sole contributor cannot be rejected from the statistical test. The excitation followed by the $\eta$ decay to the $P_{33}(1232)$ resonance should have an isospin $I = 3/2$, since the $\eta$ meson has no isospin. One may consider that the $D_{33}(1700)$ resonance contributes to this process, because it is an important resonance observed in the $\gamma p \to \pi^0 p$ reaction [15] and can decay to the $P_{33}(1232)$ resonance through $L = 0$ $\eta$ emission.

In Fig. 8, the excitation function of the cross section is shown. The solid circles represent the total cross section of
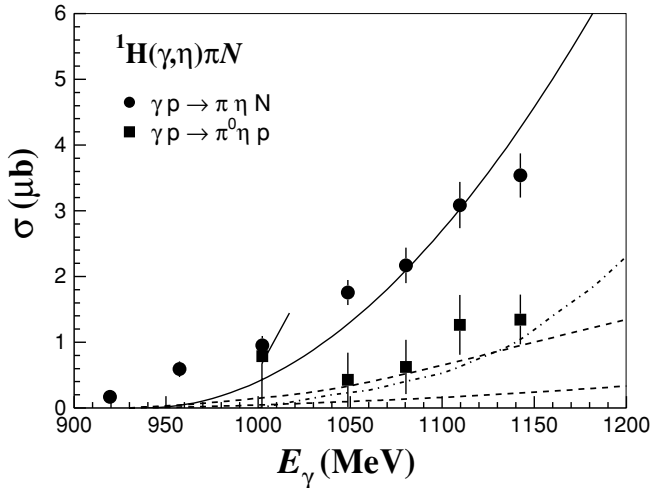
FIG. 8. Excitation function of the cross sections for the $\gamma p \to \pi \eta N$ reaction (circles) and the $\gamma p \to \pi^0 \eta p$ process (squares). Solid line corresponds to the phase space of the $\pi \eta N$ final state. Dashed and dotted-dashed lines are calculated cross sections for the $\gamma p \to \pi^0 \eta p$ process reported in [16] and [17], respectively.

the reaction $\gamma p \to \pi \eta N$, and the squares are for the reaction $\gamma p \to \pi^0 \eta p$. The latter data were deduced from the proton-accompanied $\eta$ events, and the error bars are very large because of poor statistics, as mentioned in Sec. III. Thus, one may only say that the ratio of the cross section of the $\gamma p \to \pi^0 \eta p$ process to that of the $\gamma p \to \pi^+ \eta n$ process lies between 0.5 and 1.0.

The total cross section of the reaction $\gamma p \to \pi \eta N$ increases monotonically as the photon energy increases, and it reaches almost the same value as that of the $\gamma p \to \eta p$ reaction at $E_\gamma \sim 1.15$ GeV. The solid line shows the phase space of the final $\pi \eta N$ three-body state (its magnitude is normalized at 1109 MeV) and, hence, corresponds to the cross section with a constant amplitude for process (1) as discussed above. The solid line is a poor fit to the experimental data: the phase space increases proportionally to $(E_\gamma - E_{th})^2$ above the threshold $E_{th}$, whereas the experimental data increase almost linearly with the photon energy. This suggests that the reaction proceeds through the resonance formation in the first stage of the photoabsorption and follows along either process (2) or (3). The existence of the $D_{33}(1700)$ resonance has been discussed as evidence for such a case. Besides, there are many $N^*(I = 1/2)$ resonances overlapping each other in this energy region, such as $P_{11}(1710)$, $P_{13}(1720)$, $D_{15}(1675)$, $D_{13}(1700)$, and $F_{15}(1680)$ resonances [14]. Among them, the $P_{11}(1710)$ and $D_{13}(1700)$ resonances might decay to the $S_{11}(1535)$ resonance, with $L = 0$ and 1 $\pi$ emission, respectively.

The cross section for the $\gamma p \to \pi^0 \eta p$ process is compared with the calculation by Jido *et al.* [16]. The purpose of the calculation is to test the feasibility of distinguishing the sign of

the coupling constant between the $\pi NN$ and $\pi N^* N^*$ vertices for the $S_{11}(1535)$ resonance as $N^*$; the issue is related to a chiral transformation scheme of the baryon. The result of their calculation is plotted in Fig. 8 by dashed lines: the two lines correspond to different transformation schemes. It is seen that one of the dashed lines explains the experimental data. However, the calculation includes only the $S_{11}(1535)$ resonance as an intermediate state. As already discussed, significant yields are due to process (3), presumed to be the decay sequence $D_{33}(1700) \to \eta P_{33}(1232) \to \eta \pi N$. In addition, one expects comparable yields from process (2) corresponding to the decay $N^*(I = 1/2) \to \pi S_{11}(1535) \to \pi \eta N$. Thus, more realistic calculations that include the above-mentioned processes are highly desirable to distinguish the sign of the coupling constant. In a recent paper [17], Döring *et al.* calculate the cross section of the $\gamma p \to \pi^0 \eta p$ reaction, using a chiral unitary approach for meson-baryon scattering. In their calculation, the $S_{11}(1535)$ resonance is dynamically generated, and the excitation of the $D_{33}(1700)$ resonance which subsequently decays into an $\eta$ meson and the $P_{33}(1232)$ resonance is an important process. The result also explains the experimental cross sections as shown by a dashed-dotted line in Fig. 8.

## V. CONCLUSIONS

The angular distributions and the excitation function for the $\gamma p \to \eta p$ reaction are essentially in good agreement with those reported previously. Apart from small discrepancies in the cross sections, the present results agree very well with those in [5,6]. The calculation of $\eta$-MAID [8] explains the experimental data very well except for a slight overestimate for $820 \leqslant E_\gamma \leqslant 880$ MeV.

Above $E_\gamma \geqslant 930$ MeV, the $\gamma p \to \pi \eta N$ reaction contributes increasingly to the $\eta$ emission off protons. The comparison of the momentum distributions of the $\eta$ emission with the kinematic calculations suggests that the reaction proceeds via sequential processes through the $P_{33}(1232)$ resonance $\gamma p \to \eta P_{33}(1232) \to \pi \eta N$ and the $S_{11}(1535)$ resonance, as well as via processes without intermediate resonances. The excitation function of the cross section has been deduced for the first time. The ratio of the cross section of the $\gamma p \to \pi^0 \eta p$ process to that of the $\gamma p \to \pi^+ \eta n$ process was determined to be between 0.5 and 1.0. The total cross section increases monotonically with increasing photon energy and reaches almost the same value as that of the $\gamma p \to \eta p$ reaction at $E_\gamma \sim 1.15$ GeV.

## ACKNOWLEDGMENTS

[1] B. Krusche *et al.*, Phys. Rev. Lett. **74**, 3736 (1995).

[2] A. Bock *et al.*, Phys. Rev. Lett. **81**, 534 (1998).

[3] J. Ajaka *et al.*, Phys. Rev. Lett. **81**, 1797 (1998).

[4] F. Renard *et al.* (GRAAL Collaboration), Phys. Lett. **B528**, 215 (2002).

[5] M. Duggaer *et al.* (CLAS Collaboration), Phys. Rev. Lett. **89**, 222002 (2002).

[6] V. Crede *et al.* (CB-ELSA Collaboration), Phys. Rev. Lett. **94**, 012004 (2005).

[7] B. Saghai and Z. Li, Eur. Phys. J. A **11**, 217 (2001).

[8] W. T. Chiang, S. N. Yang, L. Tiator, and D. Drechsel, Nucl. Phys. **A700**, 429 (2002).

[9] T. Kinoshita *et al.*, Phys. Lett. **B639**, 429 (2006).

[10] H. Yamazaki *et al.*, Nucl. Instrum. Methods A **536**, 70 (2005).

[11] H. Yamazaki *et al.*, Nucl. Instrum. Methods A **391**, 427 (1997).

[12] T. Yorita *et al.*, Phys. Lett. **B476**, 226 (2000).

[13] CERN Program Library.

[14] S. Eidelman *et al.* (Particle Data Group), Phys. Lett. **B592**, 1 (2004).

[15] O. Bartholomy *et al.* (CB-ELSA Collaboration), Phys. Rev. Lett. **94**, 012003 (2005).

[16] D. Jido, M. Oka, and A. Hosaka, Prog. Theor. Phys. **106**, 873 (2001).

[17] M. Döring, E. Oset, and D. Strottman, Phys. Rev. C **73**, 045209 (2006).